ACS APPLIED MATERIALS & INTERFACES

Research Article

Cite This: ACS Appl. Mater. Interfaces 2019, 11, 1384−1393

www.acsami.org

Cobalt, Nitrogen-Doped Porous Carbon Nanosheet-Assembled Flowers from Metal-Coordinated Covalent Organic Polymers for Efficient Oxygen Reduction

Shan Chen,[†] Yong Zheng,[†] Bing Zhang,[†] Yiyu Feng,[*,‡] Jixin Zhu,[§] Jingsan Xu,[∥] Chao Zhang,[*,†] Wei Feng,[‡] and Tianxi Liu[†]

[†]State Key Laboratory for Modification of Chemical Fibers and Polymer Materials, College of Materials Science and Engineering, Innovation Center for Textile Science and Technology, Donghua University, Shanghai 201620, P. R. China

[‡]School of Materials Science and Engineering, Key Laboratory of Advanced Ceramics and Machining Technology, Tianjin University, Tianjin 300072, P. R. China

[§]Shaanxi Institute of Flexible Electronics (SIFE), Northwestern Polytechnical University (NPU), 127 West Youyi Road, Xi'an 710072, P. R. China

[∥]School of Chemistry, Physics and Mechanical Engineering, Queensland University of Technology, Brisbane, Queensland 4001, Australia

Supporting Information

ABSTRACT: The breakthrough of nonprecious metal catalysts replacing platinum-based catalysts toward the oxygen reduction reaction (ORR) is extremely urgent for the development of high-efficiency energy conversation systems. Herein, a solution-processed condensation polymerization using cyanuric chloride and piperazine as the monomers was proposed for the synthesis of a nitrogen-rich covalent organic polymer (COP). High contents of precisely tailored pyridinic-N within the COP facilitate the formation of the Co/N coordination between Co ions and N species. As a result, the subsequent carbonization of the Co-coordinated COP led to the formation of the cobalt, nitrogen dual-doped porous carbon nanosheet-assembled flowers (Co/N-PCNF). The as-obtained Co/N-PCNF catalyst with a nearly 4-electron oxygen reduction pathway exhibits an excellent ORR catalytic activity with a half-wave potential of 0.835 V comparable to the commercial Pt/C catalysts (0.865 V). Most impressively, the Co/N-PCNF catalyst displays a long-term stability and a much better resistance to methanol than the Pt/C catalyst because of its high surface area, well-defined porous structure, and homogeneous distributions of active sites within the carbon matrix. Therefore, this work establishes an operating rule for tailored synthesis of COP-derived nonprecious metal catalysts offering high activity for the ORR in electrochemical energy conversations.

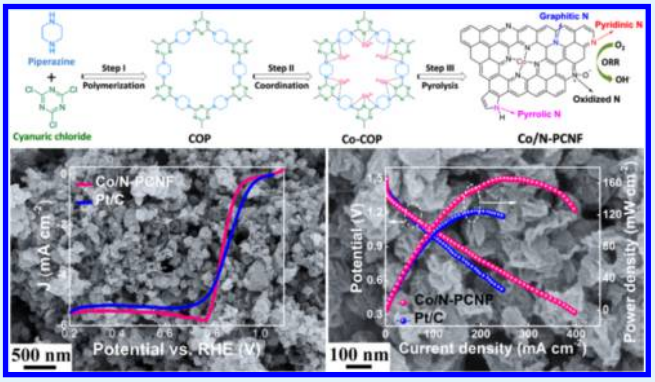

KEYWORDS: *covalent organic polymer, Co/N coordination, nitrogen doping, carbon nanosheet-assembled flower, oxygen reduction reaction*

1. INTRODUCTION

Oxygen reduction reaction (ORR) is a crucial reaction for a variety of renewable energy applications.[1−3] Platinum (Pt)-based catalysts are well-recognized as the most efficient and commercially available ORR catalysts.[4] However, the high cost and resource scarcity of Pt-based catalysts are the vital factors impeding their broad applications in energy conversion devices, especially fuel cells.[4−6] Therefore, nonprecious metal catalysts including transition metal oxides/sulfides, nitrogen-doped (N-doped) carbon, and transition metal-coordinated materials have been developed to accelerate the sluggish ORR kinetics, thus possessing the superb activity and durability for the ORR in the past few decades.[7−17]

The utilization of nonprecious metal catalysts has begun since the discovery of cobalt-supported phthalocyanine with high ORR activity,[18] followed by the finding of transition metal-containing macrocycles which can ameliorate the ORR performance with long-term stability via simple pyrolysis.[19] In addition to these macrocyclic compounds, the pyrolytic

Received: September 27, 2018
Accepted: December 12, 2018
Published: December 12, 2018

DOI: 10.1021/acsami.8b16920
ACS Appl. Mater. Interfaces 2019, 11, 1384−1393

Figure 1. Schematic of the preparation of cobalt, nitrogen dual-doped porous carbon nanosheet-assembled flowers (Co/N-PCNF).

synthesis is utilized to create nonprecious metal catalysts using the simply mixed precursors of transition metals and low-cost nitrogen-rich (N-rich) polymers.[20,21] Although these nonprecious metal catalysts have shown a relatively high catalytic ORR performance, the lack of precisely tailored active sites of transition metals and nitrogen species greatly limits the potential applications of such nonprecious metal catalysts in a broad and controllable way. Recently, the covalent organic polymers (COP) containing porphyrin rings, emerging as a new type of N-rich polymers with precisely controlled coordination sites of transition metal ions and N species, have been used as the precursors to synthesize the ORR catalysts with high catalytic performance.[22−24] However, the high cost of the porphyrin ring-containing monomers and the harsh coupling reaction conditions have greatly limited the large-scale preparation of such nonprecious metal catalysts. Therefore, the development of common, commercial, and low-cost monomers for the synthesis of COP through simple and practicable polymerization methods is urgently needed; however, still a great challenge.

Herein, we presented an efficient way to synthesize the cobalt, nitrogen dual-doped porous carbon nanosheet-assembled flowers (Co/N-PCNF) by the simple pyrolysis using cobalt ion-coordinated COP (Co/COP) as the precursor. The COP was synthesized via a typical (3 + 2) condensation polymerization using the cyanuric chlorides and piperazines as the monomers, and the abundant pyridinic-N species within the COP framework facilitate the formation of precisely arranged Co/N coordinating sites. Upon the pyrolysis, the resultant Co/N-PCNF catalysts exhibited an outstanding ORR catalytic activity, long-term stability, and excellent methanol tolerance in alkaline owning to its excellent electrical conductivity, hierarchical porous structure, and uniform-distributed active sites, indicating a promising alternate of commercial Pt/C catalysts.

2. EXPERIMENTAL SECTION

2.1. Synthesis of the COP. Cyanuric chloride (10 mmol, 1.84 g) and piperazine (15.2 mmol, 1.31 g) were fully dissolved in the tetrahydrofuran (THF) (100 mL), and then the solution was transferred to a reflux bottle. A slight excess of piperazine was added to ensure a complete reaction of cyanuric chloride. The stirring reaction was carried out at three temperature stages, namely, at ∼0 °C for 2 h, room temperature for 4 h, and 90 °C overnight. The precipitates, denoted as the COP, were filtered; washed with excess THF, ethanol, and deionized (DI) water three times, respectively; and then dried in a vacuum oven at 60 °C overnight.

2.2. Synthesis of the Co/N-PCNF. The COP (800 mg) was mixed with designed amounts of $Co(Ac)_2{\cdot}4H_2O$ by grinding using a motor for 30 min. The Co/COP-1, Co/COP-2, and Co/COP-3 represent the samples by the addition of 20, 40, and 80 mg of $Co(Ac)_2{\cdot}4H_2O$, respectively. Subsequently, the mixtures were transferred into a covered crucible and pyrolyzed at a designed temperature with a heating rate of 2 °C min^{-1} under a nitrogen flow. Upon cooling, the products were washed with 100 mL of 0.5 M H_2SO_4 for 6 h with vigorous stirring and DI water, respectively. Finally, the products were denoted as Co/N-PCNF-*x*-*T*, where *x* represents the precursors of Co/COP-*x* and *T* represents the pyrolytic temperature. For instances, the Co/N-PCNF-2-900 means the product was pyrolyzed at 900 °C using the Co/COP-2 as the precursor. For comparison, the N-PCNF-900 represents the control sample pyrolyzed at 900 °C using neat COP as the precursor.

3. RESULTS AND DISCUSSION

The synthetic route for the cobalt, nitrogen dual-doped porous carbon nanosheet-assembled flowers (Co/N-PCNF) includes three steps, as illustrated in Figure 1. First, the N-rich COP was topologically prepared by a solution-processed (3 + 2) condensation polymerization using the cyanuric chlorides and piperazines as monomers. Second, the COP was mixed with different amounts of Co salts under grinding, thus forming the unique supermolecularly assembled Co/COP complexes. The chemical structure of the Co/COP complexes with the Co/N coordination between Co ions and N-containing benzene rings is demonstrated in Figure 1. The Co/COP-1, Co/COP-2, and Co/COP-3 represent the Co/COP complexes with the Co/COP weight ratio of 1/40, 1/20, and 1/10, respectively. Third, the Co/COP precursors were pyrolyzed in a nitrogen atmosphere to obtain the Co/N-PCNF. The products were denoted as Co/N-PCNF-*x*-*T*, where *x* represents the use of Co/COP-*x* as the precursor and *T* represents the pyrolytic temperature. For instances, the Co/N-PCNF-2-900 means that the sample was pyrolyzed at 900 °C using Co/COP-2 as the precursor. For comparison, the N-PCNF-900 represents the pyrolyzed sample at 900 °C using neat COP as the precursor.

The chemical structure of the Co-coordinated COP contributes to separate individual Co sites from each other, especially upon pyrolysis, which therefore promotes the formation of uniformly dispersed Co/N active sites among the resultant Co/N-PCNF. Importantly, the pyridinic-N structure among the Co/COP precursor facilitates the formation of N-doped carbon occupying large proportions of pyridinic-N and graphitic-N upon the pyrolysis, which are favorable for boosting the ORR catalytic activity.[25]

The as-obtained COP was characterized by ^{13}C solid-state nuclear magnetic resonance (ssNMR). The ^{13}C ssNMR spectrum indicates two types of carbon structures mainly residing in the COP (Figure S1). The peaks at 45 and 164 ppm are consistent with the sp^3 and sp^2 carbon in the piperazine and triazine rings, respectively, confirming the formation of a framework with the cyanuric rings and piperazine units via condensation polymerization. X-ray diffraction (XRD) pattern of the COP shows a series of diffraction patterns in the range between 5° and 40°,

DOI: 10.1021/acsami.8b16920
ACS Appl. Mater. Interfaces 2019, 11, 1384−1393

suggesting that the as-obtained COP sample possesses a certain ordering of a framework (Figure S2). The diffraction patterns at ~6.6° and 13° can be corresponded to the faces (110) and (220) of the framework.[26] The Fourier-transform infrared (FTIR) spectrum of the COP (Figure S3a) shows typical peaks at 1490, 1300, and 2900 cm^{-1}, which correspond to the stretching vibration of C/N in triazine rings, deformation vibration of C/N in triazine rings, and stretching vibration of C/H in piperazine units, respectively. Simultaneously, the disappearance of the peak at 850 cm^{-1} implies the absence of the C/Cl bonds, further confirming the successful polymerization of the COP via the dehydrochloration. In addition, a characteristic Co/N vibration band at 1005 cm^{-1} has been observed in the Co/COP-2 sample in Figure S3b, confirming that the Co ions coordinate with the N species of the COP.[27] The X-ray photoelectron spectroscopy (XPS) spectrum for the COP is also measured in Figure S4, with the peaks assigned to binding energies of pyridinic-N (398.3 eV) and N/C tertiary amine (401.2 eV) within the COF sample.

Thermogravimetric analysis (TGA) curves of the $Co(Ac)_2 \cdot 4H_2O$, COP, and Co/COP-2 were measured in the nitrogen atmosphere (Figure S5) to guarantee the thermal stability and carbonization yield of the COP in the presence of cobalt ions. The COP shows an extremely high thermal stability even at a high temperature of 500 °C owing to its highly cross-linked structure. The weight of the COP remains an appreciable residue larger than 20 wt %, even heated to 1000 °C, suggesting that the COP is an ideal carbon precursor with an extremely high carbonization yield. Meanwhile, the Co/COP-2 shows a stronger thermal stability than the COP, especially at high temperature, further proving that the formation of the Co/COP complexes is beneficial to the full carbonization of the COP. Figure S6 depicts the nitrogen sorption/desorption isotherms and corresponding pore-size distribution of the COP, exhibiting a type-H4 isotherm with hysteretic loops, which affirms the coexistence of mesopores and micropores within the COP because of its highly cross-linked structure.

The morphologies of the COP as well the Co/COP complexes are shown in Figure 2. The COP sample exhibits a nanoflower morphology assembled with nanosheets, and these nanosheets with a smooth surface show a uniform lateral size of 100−200 nm and a thickness of ~30 nm, respectively (Figure 2a,b). However, the thicknesses of the nanosheets among the Co/COP complexes dramatically decrease with the increasing contents of Co ions within the complexes (Figure 2c−h), indicating that the Co ions coordinate well with the COP framework and thus stabilize the structural stability of the COP. The addition of Co ions also promotes the carbonization yield of the COP at high pyrolytic temperature according to TGA results. Besides, Figure S7 provides the XPS spectra of the Co/COP-1, Co/COP-2, and Co/COP-3, which reveal that the Co species are in the Co/N_x forms within the Co/COP complexes.[28]

The pyrolytic temperature plays a vital role in the ORR catalytic performance by tailoring the N contents, N forms, and graphitization degrees among the as-obtained catalysts.[29] The optimal temperatures for the preparation of the Co/N-PCNF were investigated by setting the pyrolytic temperature of 850, 900, and 950 °C, respectively. The XRD patterns in Figure 3a demonstrate the crystalline structures of the Co/N-PCNF samples obtained at different pyrolytic temperatures. Clearly, the diffraction pattern at 2θ = ~26° becomes stronger and narrower at a higher pyrolytic temperature, implying that

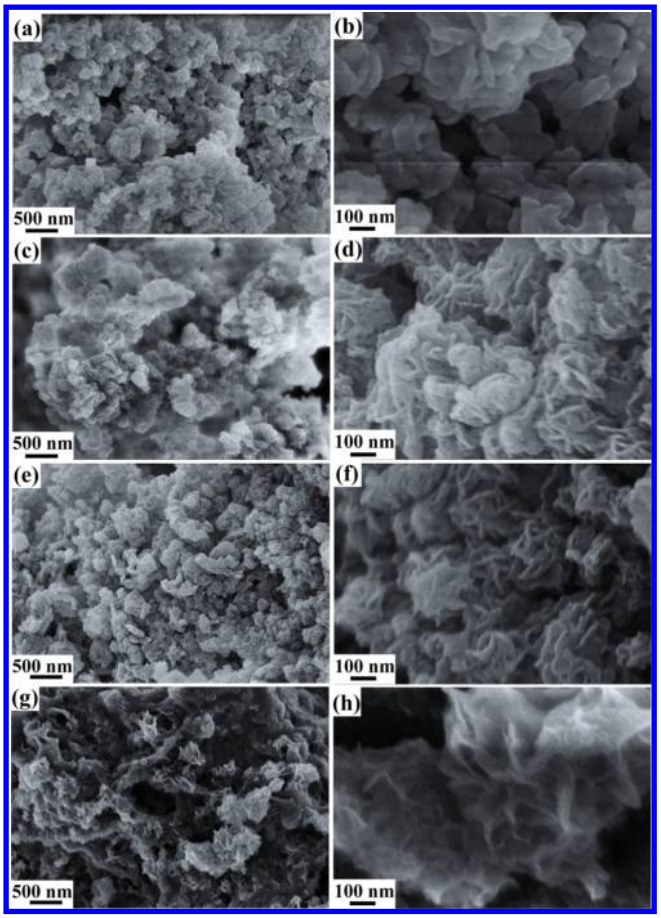

Figure 2. SEM images of (a,b) COP, (c,d) Co/COP-1, (e,f) Co/COP-2, and (g,h) Co/COP-3 at low and high magnifications, respectively.

the higher pyrolytic temperature would promote the formation of more ordered graphitic carbon structures among the Co/N-PCNF. Meanwhile, the XRD patterns at 2θ = 44°, 52°, and 76° correspond to the (111), (200), and (220) crystalline planes of the cobalt (JCPDS no. 15-0806), respectively,[30] which verify the presence of Co-based active sites in these samples. Besides, the Co/N-PCNF-2-900 sample shows a strong (111) crystalline plane, indicating more elemental Co existing in the sample prepared at the optimal temperature of 900 °C. Figure 3b depicts the Raman spectra of the Co/N-PCNF-2 samples prepared at various temperatures. The samples display two main bands called D bands (1320 cm^{-1}) and G bands (1601 cm^{-1}), which are assigned to the amorphous and graphitic carbon, respectively.[31,32] The intensity ratio of I_D/I_G of the Co/N-PCNF-2 decreases from 1.11 to 1.05 with the pyrolytic temperature rising from 850 to 950 °C. The decreased I_D/I_G value certifies the formation of more ordered graphitic structures at higher pyrolytic temperature, which is propitious to enhance electrical conductivity of the resultant catalysts.[33] Besides, the N-PCNF-900 and Co/N-PCNF-*x*-900 samples with different initial Co contents were recorded by XRD (Figures S8, S9) and Raman spectroscopy (Figure S10). The XRD patterns at 2θ = ~26° for the Co/N-PCNF-*x*-900 are consistent with the (002) diffraction planes of graphitic carbon,[31,34] suggesting that the Co/COP precursors are fully carbonized. For comparison, the diffraction pattern corresponding to the (100) diffraction plane at ~43.9° for the N-PCNF-900 is found, indicating the characteristic of disordered

DOI: 10.1021/acsami.8b16920
ACS Appl. Mater. Interfaces 2019, 11, 1384−1393

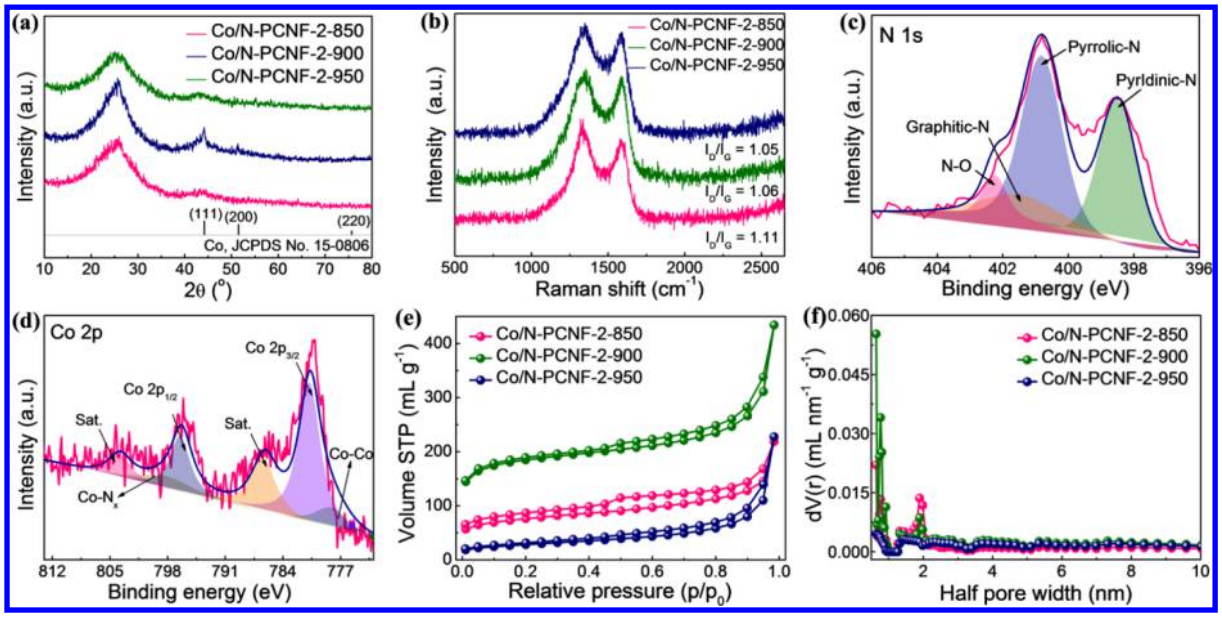

Figure 3. (a) XRD patterns and (b) Raman spectra of the Co/N-PCNF-2 prepared at different pyrolytic temperatures. (c) N 1s and (d) Co 2p XPS spectra of the Co/N-PCNF-2-900. (e) Nitrogen sorption/desorption isotherms and (f) pore-size distributions of the Co/N-PCNF-2 prepared at different pyrolytic temperatures.

carbon structures.[35] Meanwhile, the XRD patterns at 2θ = 44°, 52°, and 76° are assigned to the characteristic diffraction planes of cobalt, confirming the coexistence of cobalt active sites in the Co/N-PCNF-*x*-900. The stronger intensity of the diffraction pattern at 2θ = ~44° suggests more contents of cobalt crystalline in the Co/N-PCNF-3-900 sample. Synchronously, the XRD pattern for the Co/N-PCNF-2-900 sample with ball-milled process (30 min) prior to acid washing only reveals no significant patterns ascribing to the Co-related species (Figure S9). Figure S10 depicts that the I_D/I_G values of the Co/N-PCNF samples decrease from 1.09 to 1.03 when increasing the feeding Co contents within the Co/COP complexes, indicating that the addition of Co ions promotes the formation of more perfect graphitized carbon structure within the Co/N-PCNF samples, which are beneficial to improve electrical conductivity of the resultant catalysts. The XPS spectra announce the elemental information of the Co/N-PCNF-2-900. Figure 3c clearly reveals that the N 1s XPS spectrum can be deconvoluted into four peaks corresponding to the pyridinic-N (398.3 eV, 35.5 at. %), pyrrolic-N (400.5 eV, 42.5 at. %), graphitic-N (401.3 eV, 11.4 at. %), and N/O (402.0 eV, 10.5 at. %) species, respectively.[36−41] The pyridinic-N species among the Co/N-PCNF reveal the retaining of pyridinic-N skeletons of the Co/COP precursors, and the other types of N species are probably originated from the formation of graphitic carbon structures during carbonization. Moreover, Figure S11 shows that among the pyrolyzed samples under different temperatures, the Co/N-PCNF-2-900 has larger proportions of the graphitic-N and pyridinic-N among various N forms, which were reported to play an important role in enhancing the catalytic performance of ORR.[42] Additionally, the pyrrolic-N among the carbon structure favors the formation of active metal-coordination sites. The main three types of active N species for the ORR catalysis are of high contents in the Co/N-PCNF-2-900, which guarantee an outstanding catalytic activity. Table S1 gives the comparison of the atomic contents of Co, graphitic-N, and pyridinic-N, which are relevant to the ORR catalytic activity. The ORR active sites (mainly, Co/N, pyridinic-N, and graphitic-N) increase at the beginning and finally decrease when further increasing the pyrolytic temperature, which can be explained that the edge pyridinic-N possesses the possibility to form the Co/N coordination embedded in the as-obtained graphitic carbon layers.[42] Although the Co/N moieties are also appropriate active sites for boosting the ORR activity, the partial Co/N moieties are unfortunately covered by collapsed carbon structures because of the further increased pyrolytic temperature. Thus, these partial Co/N groups do not play a catalytic role during the ORR kinetic process. Besides, the total active sites decrease with the increase of the pyrolytic temperature. Therefore, an optimal pyrolytic temperature of 900 °C is crucial to form suitable active sites beneficial to the ORR performance. The Co 2p spectrum for the Co/N-PCNF-2-900 is demonstrated in Figure 3d, and the peak observed at 779.8 eV is attributed to the existence of Co/Co bonds. Similarly, the binging energy at nearly 796.2 and 782.6 eV correspond to Co $2p_{1/2}$ and Co $2p_{3/2}$, respectively.[43,44] The peaks at 785.2 and 802.7 eV correspond to shakeup satellites.[45] In particular, the binging energy at 798.1 eV is consistent with the Co/N_x, which is regarded as effective active sites for the ORR according to previous reports.[46] Besides, the C 1s spectra (Figure S12) can be deconvoluted into C/N (9.37 at. %) and C═N (7.15 at. %), indicating that the two types of C/N/C═N bonds contribute to the ORR performance. The Brunauer−Emmet−Teller (BET) analysis is used to calculate the specific surface area of the Co/N-PCNF-2-T. The nitrogen sorption/desorption isotherms (Figure 3e) exhibit a type-H4 isotherm with hysteretic loops in the high-pressure areas and a type-H1 in the low-pressure areas with typical slit-shaped pores, implying the coexistences of mesopores and micropores in these samples. The Co/N-PCNF-2-900 owns a high surface area of 578 $m^2\ g^{-1}$. However, the sharp decrease of the surface area for the Co/N-PCNF-2-950 (87 $m^2\ g^{-1}$) owns to collapsing of pores at a relatively high pyrolytic temperature. In addition, the density functional theory analysis is performed in Figure 3f, and the results show that the pore sizes lie in an

DOI: 10.1021/acsami.8b16920
ACS Appl. Mater. Interfaces 2019, 11, 1384−1393

Table 1. Comparison of BET Surface Area, Pore Volume, and Nitrogen Content of the COP, N-PCNF-900, and Co/N-PCNF Samples

samples	BET surface area [m^2 g^{-1}]	micropore volume [mL]	mesopore volume [mL]	total pore volume [mL]	nitrogen content [at. %]
COP	117	0.04	0.24	0.28	
N-PCNF-900	426	0.18	0.22	0.40	5.8
Co/N-PCNF-1-900	495	0.20	0.26	0.46	6.6
Co/N-PCNF-2-900	578	0.24	0.24	0.48	6.4
Co/N-PCNF-3-900	470	0.19	0.25	0.44	5.7
Co/N-PCNF-2-850	262	0.01	0.23	0.24	9.7
Co/N-PCNF-2-950	86	0.03	0.18	0.21	5.5

extremely narrow range mainly concentrated at ~1.8 nm (micropores) and few more than 2 nm (mesopores), indicating that the samples mainly have the pore form of micropores. Meanwhile, the nitrogen sorption/desorption isotherms of the Co/N-PCNF-*x*-900 were also analyzed. Figure S13a demonstrates that the obtained catalysts mainly display a typical type-IV isotherm, indicating that its porous structure is similar to that of the Co/N-PCNF-2-900. The specific surface areas are 426, 495, 578, and 470 m^2 g^{-1} for the N-PCNF-900, Co/N-PCNF-1-900, Co/N-PCNF-2-900, and Co/N-PCNF-3-900, respectively. The pore-size distributions of the Co/N-PCNF-*x*-900 in Figure S13b indicate that the optimized mass ratio of the Co ions and COP within Co/COP complexes is determined to be 1/20 for the Co/N-PCNF-2-900. Therefore, the Co/N-PCNF-2-900 contains more micropores, larger pore volumes, and better well-defined hierarchical structures than other samples, which are in favor of high-performance ORR activity.[47] The differences of the BET surface areas, pore volumes, and nitrogen contents for the COP and Co/N-PCNF catalysts can be found in Table 1. The N contents in all of these Co/N-PCNF samples are still very high (more than 5.5 at. %), although the N contents are already much less than that of the COP precursors because the carbonization could lead to inevitable losses of N species. The tailored N components in the Co/N-PCNF-2-900 are fully exposed as active sites for promoting the ORR performance because of its high surface area and well-defined porous structure.

The morphological evolution of the Co/N-PCNF-*x*-900 affected by different Co contents and pyrolytic temperatures was also investigated by the scanning electron microscopy (SEM) observations (Figure 4). No obvious nanoflower morphology could be observed for the N-PCNF-900 sample, whereas all of the Co/N-PCNF-*x*-900 samples with the addition of Co ions show the morphology of nanoflowers, confirming that the Co/COP complexes could provide an extremely stable structure upon pyrolysis. Despite the fact that Co/N-PCNF-*x*-900 possesses similar surface area values, the morphologies of these Co/N-PCNF-*x*-900 samples are quite different. The resultant Co/N-PCNF-2-900 inherits the nanoflower morphology with well-defined nanosheet assemblies, whereas the others show poor connections between individual nanoflowers. Besides, the sizes and thicknesses of the nanosheets among the Co/COP-*x*-900 samples further decrease owing to the decomposition of carbon skeletons during the formation of hierarchical holes (Figure 4a–f); interestingly, the more contents of Co doping in these samples, the better connections between these nanoflower-like structures (Figure 4a–f), which are beneficial for the electron and proton transfer. Nevertheless, further increases of Co doping bring nanosheet-assembled nanoflowers into severe aggregations during pyrolysis (Figure 4g,h), causing the violent

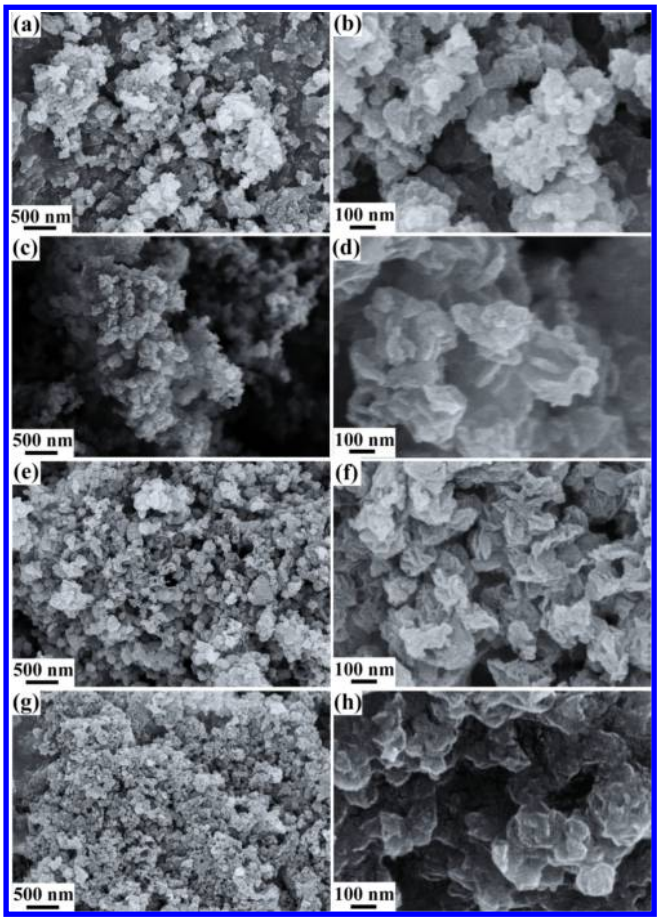

Figure 4. SEM images of (a,b) N-PCNF-900, (c,d) Co/N-PCNF-1-900, (e,f) Co/N-PCNF-2-900, and (g,h) Co/N-PCNF-3-900 at low and high magnifications, respectively.

decrease of surface areas and active sites, which are detrimental to the ORR behaviors. Meanwhile, Figure 4e,f shows that the Co/N-PCNF-2-900 presents an efficiently well-defined connection between each flower structures.

Transmission electron microscopy (TEM) images of the Co/N-PCNF-2-900 indicate that the Co/N-PCNF-2-900 maintains a nanoflower morphology with orderly stacked carbon nanosheets (Figure 5a). The ordered connections between individual carbon nanoflowers are further affirmed by Figure 5b, which could offer an outstanding conductivity. In addition, the high-resolution TEM (HRTEM) image from Figure 5c reveals that the Co/N-PCNF-2-900 has converted into the graphitic carbon with strong orientations of (002) graphitic domains with a lattice fringe spacing of 0.34 nm,[48] suggesting that the Co/N-PCNF-2-900 holds a high graphitization degree consistent with Raman results. Besides,

DOI: 10.1021/acsami.8b16920
ACS Appl. Mater. Interfaces 2019, 11, 1384–1393

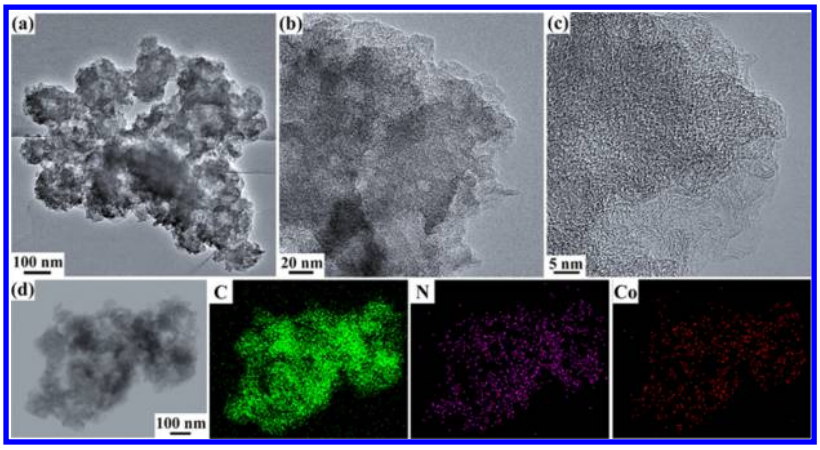

Figure 5. (a,b) TEM and (c) HRTEM images of the Co/N-PCNF-2-900. (d) TEM-EDX elemental mapping of the Co/N-PCNF-2-900 for the C, N, and Co, respectively.

the TEM-coupled energy-dispersive spectrometer (TEM–EDS) measurement is employed to investigate the elemental distributions of the Co/N-PCNF-2-900 (Figure 5d). Uniform distributions of C, N, and Co elements can be observed throughout the Co/N-PCNF-2-900, indicating a successful coordination reaction between the Co and COP to form the Co/COP precursors as well as the resultant Co/N-PCNF.

Despite the fact that the Co/N-PCNF-2-850 remains a nanosheet-assembled flowerlike nanostructure (Figure 6a,b),

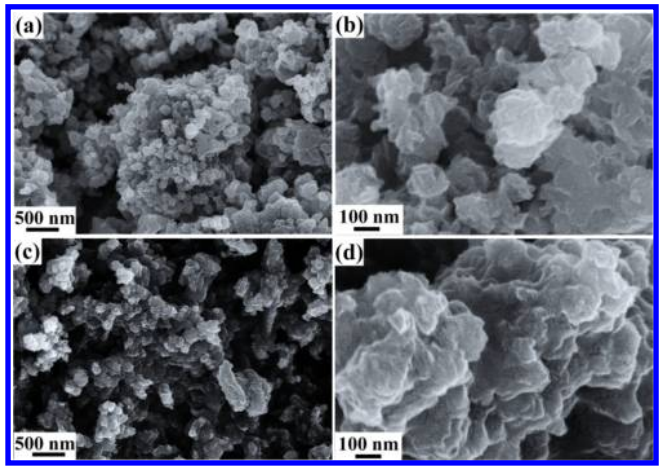

Figure 6. SEM images of (a,b) Co/N-PCNF-2-850 and (c,d) Co/N-PCNF-2-950.

the Co/N-PCNF-2-850 displays poor links among nanoflakes and thus leads to poor conductivity compared with the Co/N-PCNF-2-900. The well-defined nanoflower structures for the Co/N-PCNF-2-950 disappear, agglomerating into random structures (Figure 6c,d), which reveal a destroyed structure because of an excessive pyrolysis at an overhigh temperature.

Cyclic voltammetry (CV) measurements were performed for evaluating the ORR performance of the Co/N-PCNF-2-900 catalyst in 0.1 M O_2- and N_2-saturated KOH, respectively (Figure 7a). The CV curves of the Co/N-PCNF-2-900 show a quasi-rectangular shape in the N_2-saturated electrolyte, and a distinct oxygen reduction peak at the potential of 0.79 V versus RHE in O_2-saturated electrolyte is observed, whereas no oxygen reduction peak is found in the N_2-saturated electrolyte. Obviously, the Co/N-PCNF-2-900 offers a considerable catalytic performance for the ORR. The linear sweep voltammetry (LSV) curves of the Co/N-PCNF-2-*T* are measured in 0.1 M O_2-saturated KOH at a rotation rate of 1600 rpm. Figure 7b reveals that the Co/N-PCNF-2-900 catalyst shows a high half-wave potential of 0.835 V, only 30 mV deviations from Pt/C catalyst, which is probably because of its high surface area and more exposed active sites. In addition, the diffusion-limiting current density of the Co/N-PCNF-2-900 is greatly higher than that of Pt/C catalyst, implying an excellent ORR performance for the Co/N-PCNF-2-900 catalyst. However, the Co/N-PCNF-2-850 and Co/N-PCNF-2-950 samples show the decreased performance compared with the Co/N-PCNF-2-900 catalyst, which can be explained as poor electrical conductivities and decreased porous structures, respectively. To understand more about the reaction kinetics of the Co/N-PCNF-2-900 catalyst, LSV curves of the Co/N-PCNF-2-900 at different rotating speeds from 800 to 2400 rpm were carried out in 0.1 M O_2-saturated KOH at a scan rate of 10 mV s^{-1}. Figure 7c displays that the faster the rotation speeds, the greater the diffusion limiting current densities, telling that the ORR process is an absolutely kinetics-controlled process. The corresponding Koutecky–Levich (K–L) plots of the Co/N-PCNF-2-900 catalyst under different potentials demonstrate a great linearity and parallelism (Figure 7d), indicating a similar electron-transfer process. The electron-transfer number was calculated from 0.6 to 0.8 V versus RHE according to the K–L plots. The electron-transfer numbers at different potentials are displayed (Figure 7e), from which the average electron-transfer number is calculated to be 3.95, suggesting a nearly perfect four-electron-transfer process during the oxygen reduction. Simultaneously, the performance of the Co/N-PCNF-*x*-900 catalysts is also recorded. Figure 7f displays that the Co/N-PCNF-2-900 catalyst exhibits a more prominent catalytic behavior than those of other Co/N-PCNF-*x*-900 catalysts, indicating that the contents of Co doping greatly influence the ORR performance. An excellent performance might result from a suitable Co doping, which could also tailor the graphitization structures of the resultant carbon-based materials. Furthermore, the Co doping could enhance the active sites of the Co/N toward the ORR. However, excessive Co doping would decrease the surface area according to the BET data, which would cause the decline of exposed active sites. To further explain the excellent catalytic performance, the rotating ring-disk electrode (RRDE) test for the Co/N-PCNF-2-900 catalyst was analyzed and

DOI: 10.1021/acsami.8b16920
ACS Appl. Mater. Interfaces 2019, 11, 1384–1393

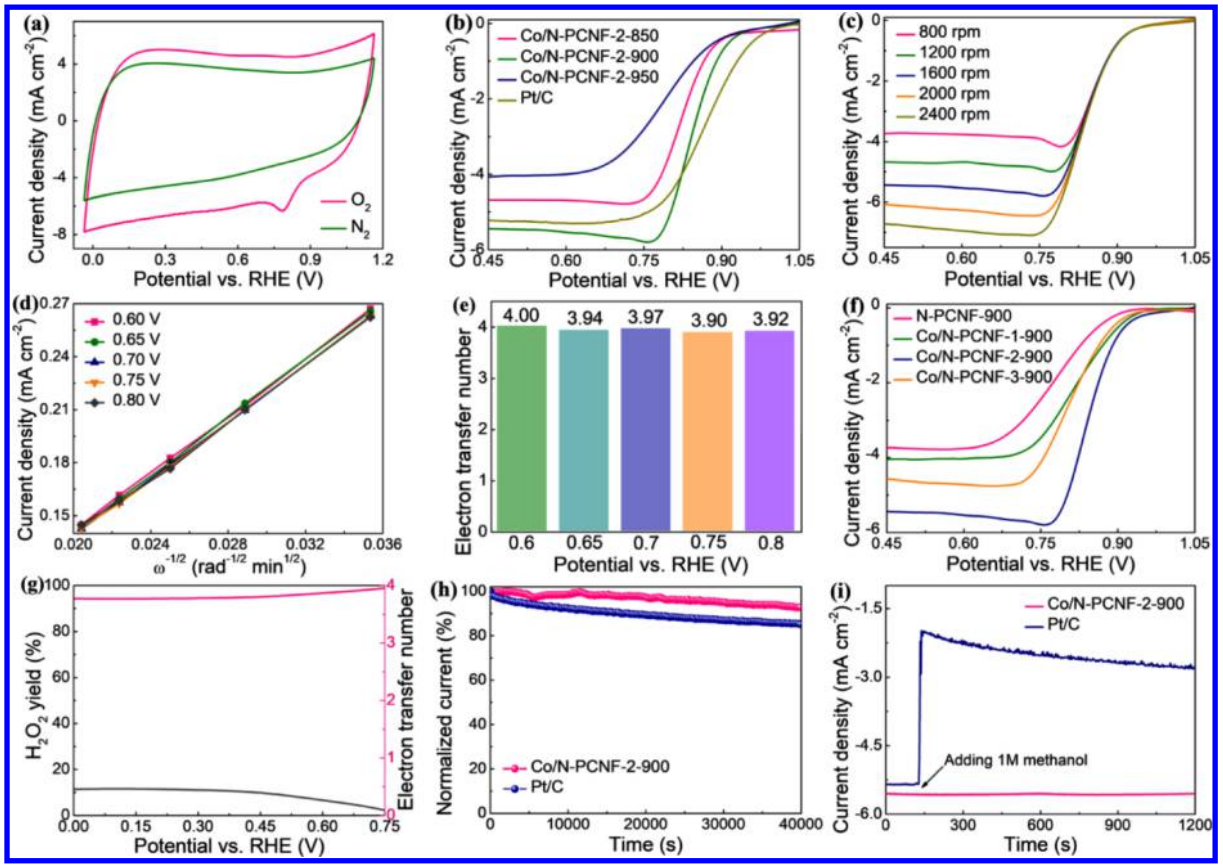

Figure 7. (a) CV curves of the Co/N-PCNF-2-900 catalyst in 0.1 M N_2- and O_2-saturated KOH, respectively. (b) LSV curves of the Co/N-PCNF-2 prepared at different pyrolytic temperatures and Pt/C in 0.1 M O_2-saturated KOH, at 1600 rpm. (c) LSV curves of the Co/N-PCNF-2-900 catalyst in 0.1 M O_2-saturated KOH at different rotation rates. (d) K−L plots and (e) calculated electron-transfer numbers of the Co/N-PCNF-2-900 derived from the current density at a potential range of 0.60−0.80 V. (f) LSV curves of the N-PCNF-900, Co/N-PCNF-1-900, Co/N-PCNF-2-900, and Co/N-PCNF-3-900 in 0.1 M O_2-saturated KOH, 1600 rpm. (g) H_2O_2 yields and calculated electron-transfer numbers of the Co/N-PCNF-2-900 derived from RRDE polarization curves in 0.1 M O_2-saturated KOH, 1600 rpm. (h) Durability of the Co/N-PCNF-2-900 at 0.664 V, 1600 rpm. (i) Chronoamperometric responses of the Pt/C and Co/N-PCNF-2-900 with the addition of 1 M methanol in 0.1 M O_2-saturated KOH at 0.664 V, 1600 rpm.

demonstrated in Figure 7g. According to the RRDE measurement, the hydrogen peroxide yields are extremely low at ∼11.4% and the electron-transfer numbers are close to four at potential intervals of 0−0.75 V versus RHE, which further demonstrate the superior performance of the Co/N-PCNF catalyst toward the ORR. The ORR activity of the Co/N-PCNF-2-900 catalyst in acid electrolyte (1 M $HClO_4$) and the catalyst with deep acid treatments were both studied (Figures S14 and S15). The Co/N-PCNF-2-900 catalyst also shows the satisfying ORR catalytic performance in the acid electrolyte, although the performance is worse than that of Pt/C. The ball-milled processes prior to acid treatment would substantially degrade the ORR performance of the Co/N-PCNF-2-900 catalyst, indicating that the elemental Co existing in the sample is beneficial to the ORR catalytic performance.

What is impressive is that the Co/N-PCNF-2-900 catalyst provides an excellent ORR performance than most of the nonprecious metal catalysts in literatures (summarized in Table 2), showing its great potential applications in energy conversion. The chronoamperometric measurements were collected at 0.664 V versus RHE at the rotation rate of 1600 rpm in 0.1 M O_2-saturated KOH. After a continuous operation for 40 000 s, a 94% of the current density remains (Figure 7h), confirming that the Co/N-PCNF-2-900 holds more superb cycling stability than that of Pt/C catalysts. Considering that methanol at the anode would occasionally penetrate into the cathode through the membrane and seriously influence the ORR performance of catalysts in methanol fuel cells, the methanol crossover effect should be seriously considered.[40] The tolerance of the Co/N-PCNF-2-900 and Pt/C catalysts against methanol poisoning was studied (Figure 7i). After adding 1 M methanol, almost no obvious current variations are noticed for the Co/N-PCNF-2-900 catalyst, whereas the Pt/C catalyst exhibits a distinct decrease of current down to nearly zero. The results clearly suggest that our Co/N-PCNF-2-900 catalyst provides a greatly enhanced tolerance to the crossover effect of methanol compared with that of the Pt/C.

As a proof of concept, a piece of carbon cloth loaded with the Co/N-PCNF-2-900 catalyst acting as an air cathode was assembled for a primary Zn−air battery. A 6 M KOH solution containing 0.2 M zinc acetate was used as the electrolyte, and a polished Zn plate was used as the anode. The primary Zn−air battery using the Co/N-PCNF-2-900 as the cathode delivers an open circuit voltage of 1.43 V and a current density at ∼250 mA cm^{-2} at the voltage of 0.67 V. The highest power density for the as-assembled battery at 250 mA cm^{-2} reaches 168 mW cm^{-2}, which is significantly higher than that of commercial Pt/C catalysts (Figure 8a). The Co/N-PCNF-2-900 catalyst is regarded as a promising cathode material for a high-power-density primary Zn−air battery ascribing to its superb catalytic

DOI: 10.1021/acsami.8b16920
ACS Appl. Mater. Interfaces 2019, 11, 1384−1393

Table 2. Summary of ORR Electrochemical Parameters of Co/N-PCNF-2-900 with Carbon Hybrid Materials in the Literature

	shifts vs $E_{1/2}$ of Pt/C (mV)			
catalysts	half-wave potential	onset potential	electron-transfer number	refs
NPMC-1000	0	−5	4	49
CoPOP-800/C	−10	−25	3.85−4	24
Co_9S_8@CNS900	−10	−20	3.91−3.99	50
N,S-PGN-700	−30	−35	3.9−4	51
N/S-2DPC-60	−60	−50	4	40
L-CCNTs-Co-800	0	−15	4	52
Fe/N/C-800	−10	−33	3.96	20
CoO@Co/N-rGO	−15	−25	4	37
NCNT/CoO−NiO−NiCo	−5	−10	3.85	53
Fe/N-doped carbon capsules	−5	−40	3.8	54
Co_3O_4−N-rmGO	−5		4	1
Fe_3C/C-800	−15	−50	3.5−4	55
N-doped holey carbon	−60	−70	3.9	56
mesoporous N-carbon	−50		4.1	57
M-CMP2-800	−11	−15	3.8	58
Co/N-PCNF-2-900	−30	−15	3.9−4.0	this work

performance and long-term durability for ORR. Meanwhile, the galvanostatic discharge curves of the Co/N-PCNF-2-900 and Pt/C catalysts were provided to evaluate the battery performance of the as-assembled Zn−air battery. As shown in Figure 8b, the Zn−air battery using the Co/N-PCNF-2-900 as the air cathode shows a stable and high voltage window of ∼1.18 V without obvious degradations, which is better than that of the Pt/C catalyst. Besides, the specific capacity of the Zn−air battery using the Co/N-PCNF-2-900 air cathode is over 810 mA h kg^{-1} at the current density of 20 mA cm^{-2} that is normalized to the mass of consumed Zn plate, which is superb to the Pt/C of 728 mA h kg^{-1} at the same current density. Figure 8c offers the discharge potential plains of the Zn−air batteries using the Co/N-PCNF-2-900 and Pt/C air electrodes, respectively, at the increasing current densities of 10, 20, 30, 40, 50, and then back to 10 mA cm^{-2}. The Zn−air battery using the Co/N-PCNF-2-900 air cathode exhibits an excellent rate performance than that of the Pt/C-based air cathode.

4. CONCLUSIONS

In summary, we have demonstrated a simple and efficient method to fabricate high-N-content COP with periodical Co/N coordination species. Upon simple pyrolysis, the as-obtained Co/N-PCNF-2-900 catalyst exhibits a fast ORR kinetics activity, with a higher durability and tolerance to methanol than that of the commercial Pt/C catalysts in alkaline. As a demonstration, the assembled primary Zn−air battery using the Co/N-PCNF-2-900 as the air cathode delivers a high powder density of 168 mW cm^{-2} and a specific capacity of 810 mA h g^{-1}, indicating a promising candidate to replace the commercial Pt/C catalyst for the ORR. The largely exposed active sites of the N and Co dual-doping within the Co/N-PCNF-2-900 catalyst greatly influences the resultant ORR activity. This work thus offers a strategy to synthesize precisely tailored Co/N dual-doped carbon materials with high catalytic activity and long-term stability toward next-generation energy conversations.

■ ASSOCIATED CONTENT

Supporting Information

The Supporting Information is available free of charge on the ACS Publications website at DOI: 10.1021/acsami.8b16920.

Experimental section; solid-state 13C NMR spectra for the COP; solid-state ^{13}C NMR spectra and XRD pattern of the COP; FTIR spectra of COP and Co/COP-2; N 1s XPS spectra of COP; TGA curves of $Co(Ac)_2{\cdot}4H_2O$, COP, and Co/COP-2; nitrogen adsorption/desorption isotherms and pore-size distributions of COP; XPS spectra of Co/COP-1, Co/COP-2, and Co/COP-3; XRD patterns of N-PCNF-900, Co/N-PCNF-1-900, Co/N-PCNF-2-900, CoN-PCNF-3-900, and Co/N-PCNF-2-900 with conventional acid washing and ball milling prior to acid washing; Raman spectra of N-PCNF-900, Co/N-PCNF-1-900, Co/N-PCNF-2-900, and Co/N-PCNF-3-900; N 1s XPS spectra of Co/N-PCNF-2-850, Co/N-PCNF-2-900, and Co/N-PCNF-2-950; C 1s XPS spectra for Co/N-PCNF-2-900; nitrogen adsorption/desorption isotherms and pore-size distributions of N-PCNF-900 and Co/N-PCNF-*x*-900 samples; LSV curves of Co/N-PCNF-2-900 and Pt/C in 0.1 M $HClO_4$; LSV curves for Co/N-PCNF-2-900 with conventional acid washing and ball milling prior to acid washing in 0.1 M KOH; and comparison of the atomic content of Co, graphitic-N, and pyridinic-N for the Co/N-PCNF samples (PDF)

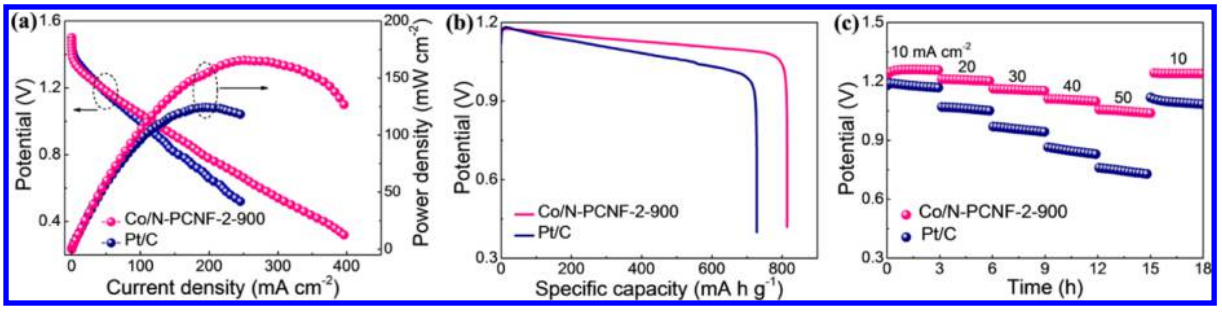

Figure 8. Battery performance of the primary Zn−air batteries. (a) Discharge polarization curves and power densities of the Co/N-PCNF-2-900 and Pt/C electrodes, respectively. (b) Galvanostatic discharge curves of the Co/N-PCNF-2-900 and Pt/C electrodes at the current density of 20 mA cm^{-2}, respectively. (c) Rate performance of the Co/N-PCNF-2-900 and Pt/C electrodes at the current density of 10, 20, 30, 40, 50, and 10 mA cm^{-2}, respectively.

DOI: 10.1021/acsami.8b16920
ACS Appl. Mater. Interfaces 2019, 11, 1384−1393

AUTHOR INFORMATION

Corresponding Authors

*E-mail: fengyiyu@tju.edu.cn (Y.F.).
*E-mail: czhang@dhu.edu.cn (C.Z.).

ORCID

Yiyu Feng: 0000-0002-1071-1995
Jixin Zhu: 0000-0001-8749-8937
Jingsan Xu: 0000-0003-1172-3864
Chao Zhang: 0000-0003-1255-7183
Wei Feng: 0000-0002-5816-7343
Tianxi Liu: 0000-0002-5592-7386

Notes

The authors declare no competing financial interest.

ACKNOWLEDGMENTS

We are grateful for the financial support from the National Natural Science Foundation of China (51433001, 21504012, and 51773035), the Shanghai Rising-Star Program (18QA1400200), the Natural Science Foundation of Shanghai (17ZR1439900), the Program of Shanghai Subject Chief Scientist (17XD1400100), and the Shanghai Scientific and Technological Innovation Project (18JC1410600).

REFERENCES

(1) Liang, Y.; Li, Y.; Wang, H.; Zhou, J.; Wang, J.; Regier, T.; Dai, H. Co3O4 Nanocrystals on Graphene as a Synergistic Catalyst for Oxygen Reduction Reaction. *Nat. Mater.* **2011**, *10*, 780−786.

(2) Shao, M.; Chang, Q.; Dodelet, J.-P.; Chenitz, R. Recent Advances in Electrocatalysts for Oxygen Reduction Reaction. *Chem. Rev.* **2016**, *116*, 3594−3657.

(3) Wu, G.; Zelenay, P. Nanostructured Nonprecious Metal Catalysts for Oxygen Reduction Reaction. *Acc. Chem. Res.* **2013**, *46*, 1878−1889.

(4) Marković, N. M.; Schmidt, T. J.; Stamenković, V.; Ross, P. N. Oxygen Reduction Reaction on Pt and Pt Bimetallic Surfaces: A Selective Review. *Fuel Cells* **2001**, *1*, 105−116.

(5) Xie, B.; Zhang, Y.; Zhang, R. Coassembly and High ORR Performance of Monodisperse Pt Nanocrystals with a Mesopore-Rich Nitrogen-Doped Graphene Aerogel. *J. Mater. Chem. A* **2017**, *5*, 17544−17548.

(6) Huang, Z.; Li, L.; Wang, Y.; Zhang, C.; Liu, T. Polyaniline/Graphene Nanocomposites Towards High-Performance Supercapacitors: A Review. *Compos. Commun.* **2018**, *8*, 83−91.

(7) Yang, L.; Cheng, D.; Xu, H.; Zeng, X.; Wan, X.; Shui, J.; Xiang, Z.; Cao, D. Unveiling the High-Activity Origin of Single-Atom Iron Catalysts for Oxygen Reduction Reaction. *Proc. Natl. Acad. Sci. U.S.A.* **2018**, *115*, 6626.

(8) Dai, L.; Xue, Y.; Qu, L.; Choi, H.-J.; Baek, J.-B. Metal-Free Catalysts for Oxygen Reduction Reaction. *Chem. Rev.* **2015**, *115*, 4823−4892.

(9) Yin, P.; Yao, T.; Wu, Y.; Zheng, L.; Lin, Y.; Liu, W.; Ju, H.; Zhu, J.; Hong, X.; Deng, Z.; Zhou, G.; Wei, S.; Li, Y. Single Cobalt Atoms with Precise N-Coordination as Superior Oxygen Reduction Reaction Catalysts. *Angew. Chem., Int. Ed.* **2016**, *55*, 10800−10805.

(10) Liu, T.; Feng, S.; Huo, J.; Li, Q.; Xie, C.; Wang, S. Crystalline-Water/Coordination Induced Formation of 3D Highly Porous Heteroatom-Doped Ultrathin Carbon Nanosheet Networks for Oxygen Reduction Reaction. *ChemCatChem* **2018**, *10*, 4562−4568.

(11) Liu, C.; Wang, J.; Li, J.; Liu, J.; Wang, C.; Sun, X.; Shen, J.; Han, W.; Wang, L. Electrospun ZIF-Based Hierarchical Carbon Fiber as an Efficient Electrocatalyst for the Oxygen Reduction Reaction. *J. Mater. Chem. A* **2017**, *5*, 1211−1220.

(12) Hu, C.; Dai, L. Carbon-Based Metal-Free Catalysts for Electrocatalysis Beyond the ORR. *Angew. Chem., Int. Ed.* **2016**, *55*, 11736−11758.

(13) Yang, L.; Zeng, X.; Wang, W.; Cao, D. Recent Progress in Mof-Derived, Heteroatom-Doped Porous Carbons as Highly Efficient Electrocatalysts for Oxygen Reduction Reaction in Fuel Cells. *Adv. Funct. Mater.* **2017**, *28*, 1704537.

(14) Yu, H.; Fisher, A.; Cheng, D.; Cao, D. Cu,N-Codoped Hierarchical Porous Carbons as Electrocatalysts for Oxygen Reduction Reaction. *ACS Appl. Mater. Interfaces* **2016**, *8*, 21431−21439.

(15) Bu, Y.; Gwon, O.; Nam, G.; Jang, H.; Kim, S.; Zhong, Q.; Cho, J.; Kim, G. A Highly Efficient and Robust Cation Ordered Perovskite Oxide as a Bifunctional Catalyst for Rechargeable Zinc-Air Batteries. *ACS Nano* **2017**, *11*, 11594−11601.

(16) Yang, L.; Shi, L.; Wang, D.; Lv, Y.; Cao, D. Single-Atom Cobalt Electrocatalysts for Foldable Solid-State Zn-Air Battery. *Nano Energy* **2018**, *50*, 691−698.

(17) Miao, Y.-E.; Li, F.; Lu, H.; Yan, J.; Huang, Y.; Liu, T. Nanocubic-Co 3 O 4 coupled with nitrogen-doped carbon nanofiber network: A synergistic binder-free catalyst toward oxygen reduction reactions. *Compos. Commun.* **2016**, *1*, 15−19.

(18) Jasinski, R. A New Fuel Cell Cathode Catalyst. *Nature* **1964**, *201*, 1212.

(19) Ling, T.; Yan, D.-Y.; Jiao, Y.; Wang, H.; Zheng, Y.; Zheng, X.; Mao, J.; Du, X.-W.; Hu, Z.; Jaroniec, M.; Qiao, S.-Z. Engineering Surface Atomic Structure of Single-Crystal Cobalt (II) Oxide Nanorods for Superior Electrocatalysis. *Nat. Commun.* **2016**, *7*, 12876.

(20) Lin, L.; Zhu, Q.; Xu, A.-W. Noble-Metal-Free Fe-N/C Catalyst for Highly Efficient Oxygen Reduction Reaction under Both Alkaline and Acidic Conditions. *J. Am. Chem. Soc.* **2014**, *136*, 11027−11033.

(21) Wu, G.; More, K. L.; Johnston, C. M.; Zelenay, P. High-Performance Electrocatalysts for Oxygen Reduction Derived from Polyaniline, Iron, and Cobalt. *Science* **2011**, *332*, 443−447.

(22) Ma, W.; Yu, P.; Ohsaka, T.; Mao, L. An Efficient Electrocatalyst for Oxygen Reduction Reaction Derived from a Co-Porphyrin-Based Covalent Organic Framework. *Electrochem. Commun.* **2015**, *52*, 53−57.

(23) Brüller, S.; Liang, H.-W.; Kramm, U. I.; Krumpfer, J. W.; Feng, X.; Müllen, K. Bimetallic Porous Porphyrin Polymer-Derived Non-Precious Metal Electrocatalysts for Oxygen Reduction Reactions. *J. Mater. Chem. A* **2015**, *3*, 23799−23808.

(24) Lu, G.; Zhu, Y.; Xu, K.; Jin, Y.; Ren, Z. J.; Liu, Z.; Zhang, W. Metallated Porphyrin Based Porous Organic Polymers as Efficient Electrocatalysts. *Nanoscale* **2015**, *7*, 18271−18277.

(25) Wang, X.-R.; Liu, J.-Y.; Liu, Z.-W.; Wang, W.-C.; Luo, J.; Han, X.-P.; Du, X.-W.; Qiao, S.-Z.; Yang, J. Identifying the Key Role of Pyridinic-N-Co Bonding in Synergistic Electrocatalysis for Reversible ORR/OER. *Adv. Mater.* **2018**, *30*, 1800005.

(26) Zhao, H.; Jin, Z.; Su, H.; Jing, X.; Sun, F.; Zhu, G. Targeted Synthesis of a 2D Ordered Porous Organic Framework for Drug Release. *Chem. Commun.* **2011**, *47*, 6389−6391.

(27) Wu, Z.-S.; Chen, L.; Liu, J.; Parvez, K.; Liang, H.; Shu, J.; Sachdev, H.; Graf, R.; Feng, X.; Müllen, K. High-Performance Electrocatalysts for Oxygen Reduction Derived from Cobalt Porphyrin-Based Conjugated Mesoporous Polymers. *Adv. Mater.* **2013**, *26*, 1450−1455.

(28) Tang, C.; Wang, B.; Wang, H.-F.; Zhang, Q. Defect Engineering toward Atomic Co-N x -C in Hierarchical Graphene for Rechargeable Flexible Solid Zn-Air Batteries. *Adv. Mater.* **2017**, *29*, 1703185.

(29) Zhao, Y.; Watanabe, K.; Hashimoto, K. Self-Supporting Oxygen Reduction Electrocatalysts Made from a Nitrogen-Rich Network Polymer. *J. Am. Chem. Soc.* **2012**, *134*, 19528−19531.

(30) Zhang, M.; Dai, Q.; Zheng, H.; Chen, M.; Dai, L. Novel MOF-Derived Co@N-C Bifunctional Catalysts for Highly Efficient Zn-Air Batteries and Water Splitting. *Adv. Mater.* **2018**, *30*, 1705431.

(31) Tian, H.; Wang, N.; Xu, F.; Zhang, P.; Hou, D.; Mai, Y.; Feng, X. Nitrogen-Doped Carbon Nanosheets and Nanoflowers with Holey Mesopores for Efficient Oxygen Reduction Catalysis. *J. Mater. Chem. A* **2018**, *6*, 10354−10360.

DOI: 10.1021/acsami.8b16920
ACS Appl. Mater. Interfaces 2019, 11, 1384−1393

(32) Ji, B.; Zhang, F.; Song, X.; Tang, Y. A Novel Potassium-Ion-Based Dual-Ion Battery. *Adv. Mater.* **2017**, *29*, 1700519.
(33) Xu, Q.; Tang, Y.; Zhang, X.; Oshima, Y.; Chen, Q.; Jiang, D. Template Conversion of Covalent Organic Frameworks into 2D Conducting Nanocarbons for Catalyzing Oxygen Reduction Reaction. *Adv. Mater.* **2018**, *30*, 1706330.
(34) Lin, M.-C.; Gong, M.; Lu, B.; Wu, Y.; Wang, D.-Y.; Guan, M.; Angell, M.; Chen, C.; Yang, J.; Hwang, B.-J.; Dai, H. An Ultrafast Rechargeable Aluminium-Ion Battery. *Nature* **2015**, *520*, 324.
(35) Tang, K.; Fu, L.; White, R. J.; Yu, L.; Titirici, M.-M.; Antonietti, M.; Maier, J. Hollow Carbon Nanospheres with Superior Rate Capability for Sodium-Based Batteries. *Adv. Energy Mater.* **2012**, *2*, 873−877.
(36) Thomas, M.; Illathvalappil, R.; Kurungot, S.; Nair, B. N.; Mohamed, A. A. P.; Anilkumar, G. M.; Yamaguchi, T.; Hareesh, U. S. Graphene Oxide Sheathed ZIF-8 Microcrystals: Engineered Precursors of Nitrogen-Doped Porous Carbon for Efficient Oxygen Reduction Reaction (ORR) Electrocatalysis. *ACS Appl. Mater. Interfaces* **2016**, *8*, 29373−29382.
(37) Liu, X. X.; Zang, J. B.; Chen, L.; Chen, L. B.; Chen, X.; Wu, P.; Zhou, S. Y.; Wang, Y. H. A microwave-assisted synthesis of CoO@Co core-shell structures coupled with N-doped reduced graphene oxide used as a superior multi-functional electrocatalyst for hydrogen evolution, oxygen reduction and oxygen evolution reactions. *J. Mater. Chem. A* **2017**, *5*, 5865−5872.
(38) Fu, S.; Zhu, C.; Su, D.; Song, J.; Yao, S.; Feng, S.; Engelhard, M. H.; Du, D.; Lin, Y. Porous Carbon-Hosted Atomically Dispersed Iron-Nitrogen Moiety as Enhanced Electrocatalysts for Oxygen Reduction Reaction in a Wide Range of pH. *Small* **2018**, *14*, 1703118.
(39) Yang, L.; Lv, Y.; Cao, D. Co,N-Codoped Nanotube/Graphene 1D/2D Heterostructure for Efficient Oxygen Reduction and Hydrogen Evolution Reactions. *J. Mater. Chem. A* **2018**, *6*, 3926−3932.
(40) Su, Y.; Yao, Z.; Zhang, F.; Wang, H.; Mics, Z.; Cánovas, E.; Bonn, M.; Zhuang, X.; Feng, X. Sulfur-Enriched Conjugated Polymer Nanosheet Derived Sulfur and Nitrogen co-Doped Porous Carbon Nanosheets as Electrocatalysts for Oxygen Reduction Reaction and Zinc-Air Battery. *Adv. Funct. Mater.* **2016**, *26*, 5893−5902.
(41) Pels, J. R.; Kapteijn, F.; Moulijn, J. A.; Zhu, Q.; Thomas, K. M. Evolution of Nitrogen Functionalities in Carbonaceous Materials During Pyrolysis. *Carbon* **1995**, *33*, 1641−1653.
(42) Li, M.; Bo, X.; Zhang, Y.; Han, C.; Nsabimana, A.; Guo, L. Cobalt and Nitrogen Co-Embedded Onion-Like Mesoporous Carbon Vesicles as Efficient Catalysts for Oxygen Reduction Reaction. *J. Mater. Chem. A* **2014**, *2*, 11672−11682.
(43) Zhu, J.; Metzger, M.; Antonietti, M.; Fellinger, T.-P. Vertically Aligned Two-Dimensional Graphene-Metal Hydroxide Hybrid Arrays for Li-O2 Batteries. *ACS Appl. Mater. Interfaces* **2016**, *8*, 26041−26050.
(44) Liu, X.; Wang, Y.; Wang, Z.; Zhou, T.; Yu, M.; Xiu, L.; Qiu, J. Achieving ultralong life sodium storage in amorphous cobalt-tin binary sulfide nanoboxes sheathed in N-doped carbon. *J. Mater. Chem. A* **2017**, *5*, 10398−10405.
(45) Su, C.-Y.; Cheng, H.; Li, W.; Liu, Z.-Q.; Li, N.; Hou, Z.; Bai, F.-Q.; Zhang, H.-X.; Ma, T.-Y. Atomic Modulation of FeCo-Nitrogen-Carbon Bifunctional Oxygen Electrodes for Rechargeable and Flexible All-Solid-State Zinc-Air Battery. *Adv. Energy Mater.* **2017**, *7*, 1602420.
(46) Zhang, W.; Yao, X.; Zhou, S.; Li, X.; Li, L.; Yu, Z.; Gu, L. ZIF-8/ZIF-67-Derived Co-N x -Embedded 1D Porous Carbon Nanofibers with Graphitic Carbon-Encased Co Nanoparticles as an Efficient Bifunctional Electrocatalyst. *Small* **2018**, *14*, 1800423.
(47) Chung, H. T.; Cullen, D. A.; Higgins, D.; Sneed, B. T.; Holby, E. F.; More, K. L.; Zelenay, P. Direct Atomic-Level Insight into the Active Sites of a High-Performance PGM-Free ORR Catalyst. *Science* **2017**, *357*, 479−484.
(48) Jiao, L.; Hu, Y.; Ju, H.; Wang, C.; Gao, M.-R.; Yang, Q.; Zhu, J.; Yu, S.-H.; Jiang, H.-L. From Covalent Triazine-Based Frameworks to N-Doped Porous Carbon/Reduced Graphene Oxide Nanosheets: Efficient Electrocatalysts for Oxygen Reduction. *J. Mater. Chem. A* **2017**, *5*, 23170−23178.
(49) Zhang, J.; Zhao, Z.; Xia, Z.; Dai, L. A Metal-Free Bifunctional Electrocatalyst for Oxygen Reduction and Oxygen Evolution Reactions. *Nat. Nanotechnol.* **2015**, *10*, 444.
(50) Zhu, Q.-L.; Xia, W.; Akita, T.; Zou, R.; Xu, Q. Metal-Organic Framework-Derived Honeycomb-Like Open Porous Nanostructures as Precious-Metal-Free Catalysts for Highly Efficient Oxygen Electroreduction. *Adv. Mater.* **2016**, *28*, 6391−6398.
(51) Wu, M.; Liu, Y.; Zhu, Y.; Lin, J.; Liu, J.; Hu, H.; Wang, Y.; Zhao, Q.; Lv, R.; Qiu, J. Supramolecular Polymerization-Assisted Synthesis of Nitrogen and Sulfur Dual-Doped Porous Graphene Networks from Petroleum Coke as Efficient Metal-Free Electrocatalysts for the Oxygen Reduction Reaction. *J. Mater. Chem. A* **2017**, *5*, 11331−11339.
(52) Yu, L.; Yang, J. F.; Guan, B. Y.; Lu, Y.; Lou, X. W. D. Hierarchical Hollow Nanoprisms Based on Ultrathin Ni-Fe Layered Double Hydroxide Nanosheets with Enhanced Electrocatalytic Activity Towards Oxygen Evolution. *Angew. Chem., Int. Ed.* **2017**, *57*, 172−176.
(53) Liu, X.; Park, M.; Kim, M. G.; Gupta, S.; Wu, G.; Cho, J. Integrating NiCo Alloys with Their Oxides as Efficient Bifunctional Cathode Catalysts for Rechargeable Zinc-Air Batteries. *Angew. Chem., Int. Ed.* **2015**, *54*, 9654−9658.
(54) Ferrero, G. A.; Preuss, K.; Marinovic, A.; Jorge, A. B.; Mansor, N.; Brett, D. J. L.; Fuertes, A. B.; Sevilla, M.; Titirici, M.-M. Fe-N-Doped Carbon Capsules with Outstanding Electrochemical Performance and Stability for the Oxygen Reduction Reaction in Both Acid and Alkaline Conditions. *ACS Nano* **2016**, *10*, 5922−5932.
(55) Hu, Y.; Jensen, J. O.; Zhang, W.; Cleemann, L. N.; Xing, W.; Bjerrum, N. J.; Li, Q. Hollow Spheres of Iron Carbide Nanoparticles Encased in Graphitic Layers as Oxygen Reduction Catalysts. *Angew. Chem., Int. Ed.* **2014**, *53*, 3675−3679.
(56) Xiang, Z.; Cao, D.; Huang, L.; Shui, J.; Wang, M.; Dai, L. Nitrogen-Doped Holey Graphitic Carbon from 2D Covalent Organic Polymers for Oxygen Reduction. *Adv. Mater.* **2014**, *26*, 3315−3320.
(57) Yang, W.; Fellinger, T.-P.; Antonietti, M. Efficient Metal-Free Oxygen Reduction in Alkaline Medium on High-Surface-Area Mesoporous Nitrogen-Doped Carbons Made from Ionic Liquids and Nucleobases. *J. Am. Chem. Soc.* **2011**, *133*, 206−209.
(58) Yuan, K.; Zhuang, X.; Fu, H.; Brunklaus, G.; Forster, M.; Chen, Y.; Feng, X.; Scherf, U. Two-Dimensional Core-Shelled Porous Hybrids as Highly Efficient Catalysts for the Oxygen Reduction Reaction. *Angew. Chem., Int. Ed.* **2016**, *55*, 6858−6863.

DOI: 10.1021/acsami.8b16920
ACS Appl. Mater. Interfaces 2019, 11, 1384−1393